# An Interplay between Metal-Fullerene and Metal-Metal Bonding in Molecular Magnetism of Erbium Metallofullerenes

Ruslan B. Zaripov,[a]* Fupin Liu,[b,c] Marco Rosenkranz,[b] Matheus Felipe de Souza Barbosa,[b] Yuri E. Kandrashkin,[a] Vladislav Kataev,[b] Stanislav M. Avdoshenko,[b] Alexey A. Popov[b]*

## Supporting Information

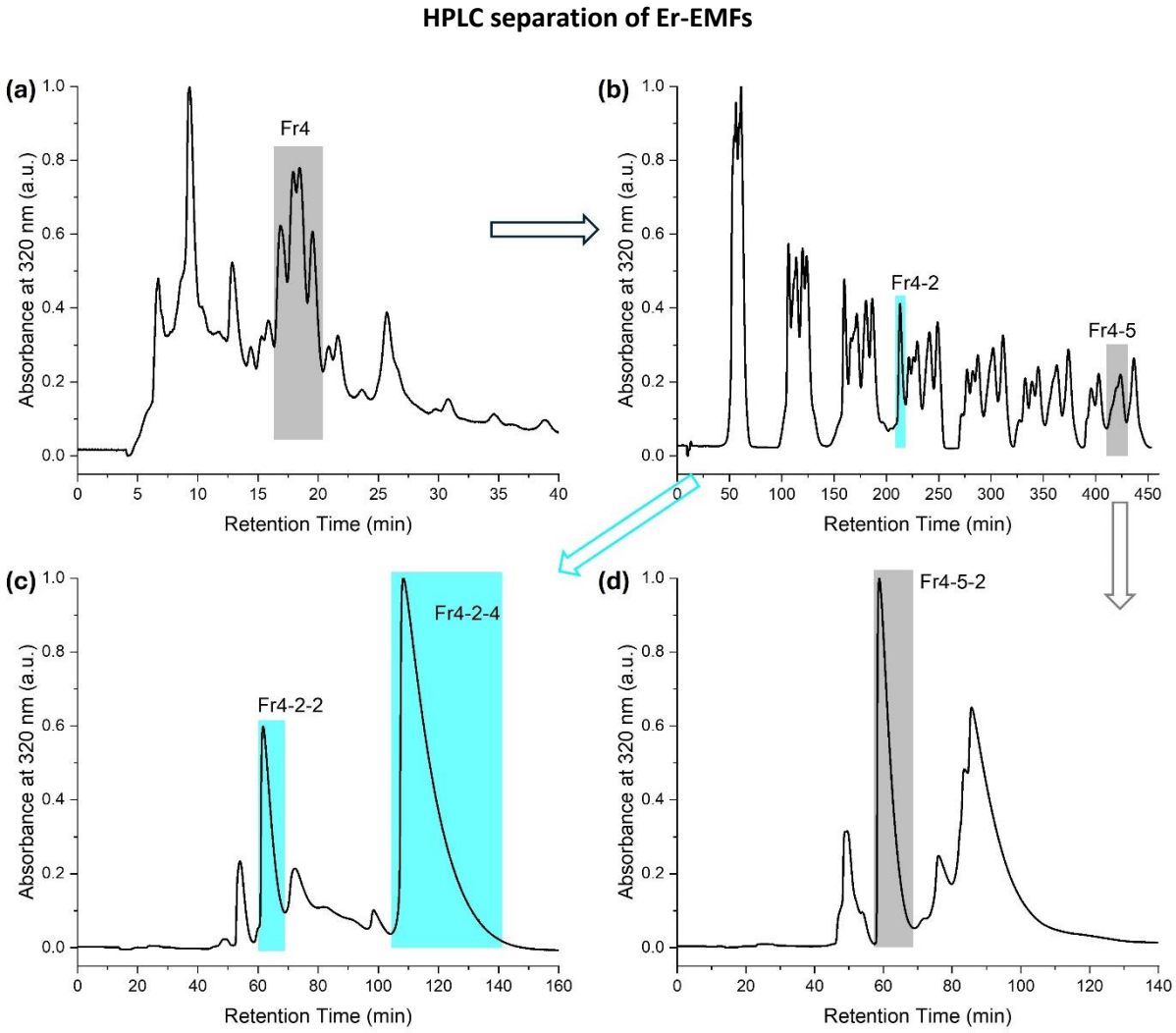


**Figure S1**. Separation of Er@$C_{80}$($CH_2Ph$), Er@$C_{82}$($CH_2Ph$), and $Er_2$@$C_{80}$($CH_2Ph$). Three steps HPLC separation were required to obtain the pure compounds. **(a)** HPLC profile of the mixture of benzyl-derivatized Er-EMFs. The highlighted fraction (Fr4) contains Er@$C_{80}$($CH_2Ph$), Er@$C_{82}$($CH_2Ph$), and $Er_2$@$C_{80}$($CH_2Ph$) was collected for further separation. HPLC conditions: linear combination of two 4.6 × 250 mm Buckyprep columns; flow rate 1.6 mL/min; injection volume 800 $\mu$L; toluene as eluent; 40 °C. **(b)** Recycling HPLC separation of the Fr4. The highlighted fractions (Fr4-2 and Fr4-5) containing Er@$C_{80}$($CH_2Ph$), Er@$C_{82}$($CH_2Ph$), and $Er_2$@$C_{80}$($CH_2Ph$), were collected for further separation (10 × 250 mm Buckyprep column; flow rate 1.5 mL/min; injection volume 4.5 mL; toluene as eluent). **(c)** HPLC separation of the Fr4-2. Pure Er@$C_{80}$($CH_2Ph$) and Er@$C_{82}$($CH_2Ph$) were obtained as Fr4-2-4 and Fr4-2-2, respectively. (10 × 250 mm Buckyprep-D column; flow rate 1.0 mL/min; injection volume 4.5 mL; toluene as eluent). **(d)** HPLC separation of the Fr4-5. Pure $Er_2$@$C_{80}$($CH_2Ph$) was obtained as Fr4-5-2. (10 × 250 mm Buckyprep-D column; flow rate 1.0 mL/min; injection volume 4.5 mL; toluene as eluent).

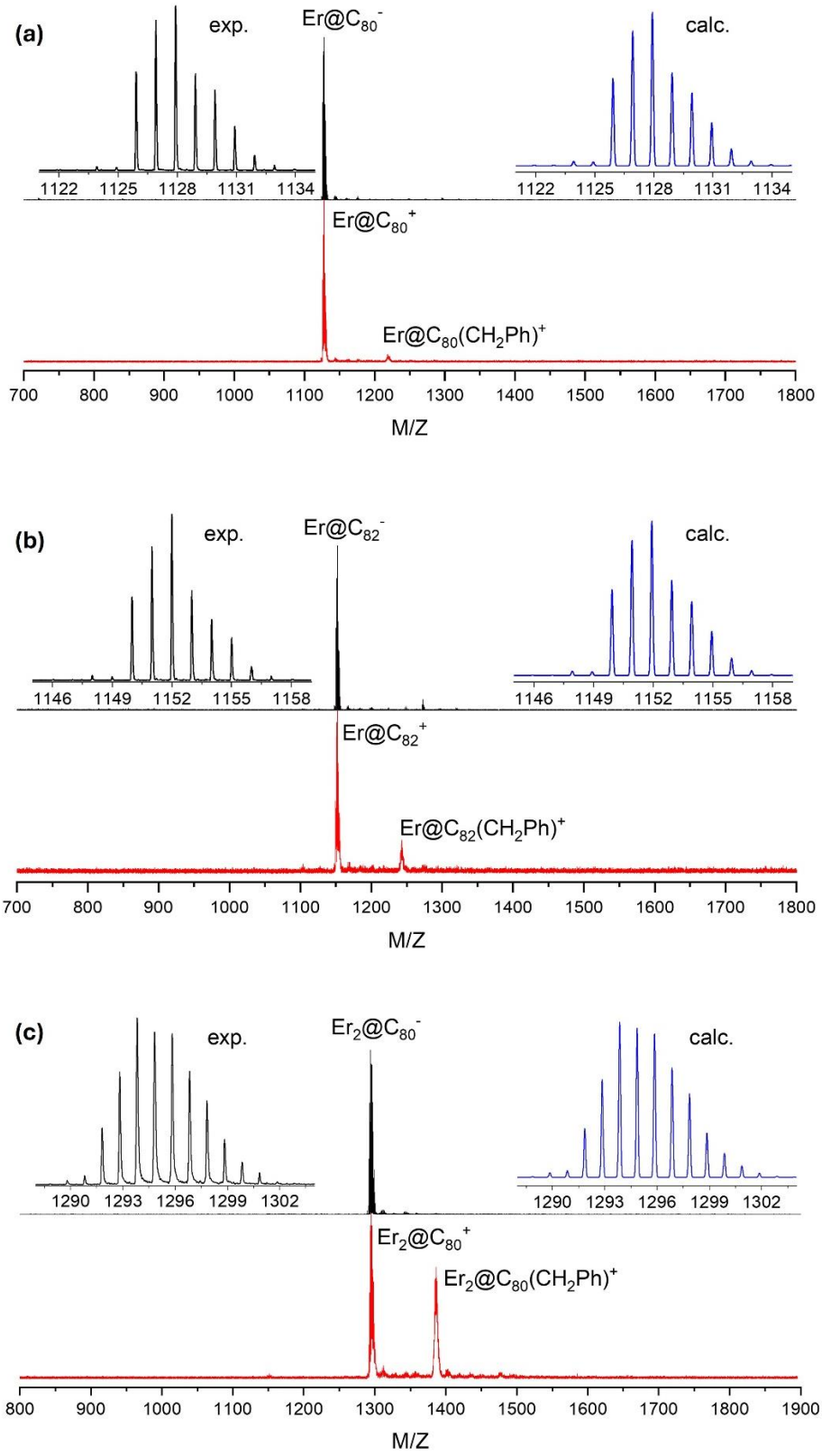


**Figure S2**. Matrix-assisted laser desorption/ionization time-of-flight (MALDI TOF) mass-spectra of **(a)** Er@$C_{80}$($CH_2$Ph), **(b)** Er@$C_{82}$($CH_2$Ph), and **(c)** $Er_2$@$C_{80}$($CH_2$Ph). Reflection negative (top) and linear positive (bottom) ionization modes, 1,1,4,4-tetraphenyl-1,3-butadiene was used as matrix. Resolution in positive mode is not high enough for analysis of isotopic distribution. In the negative ion mode, strong fragmentation does not allow for detection of molecular peak, but spectral resolution is sufficient to prove correct isotopic distribution of the Er-EMF$^-$ fragments.

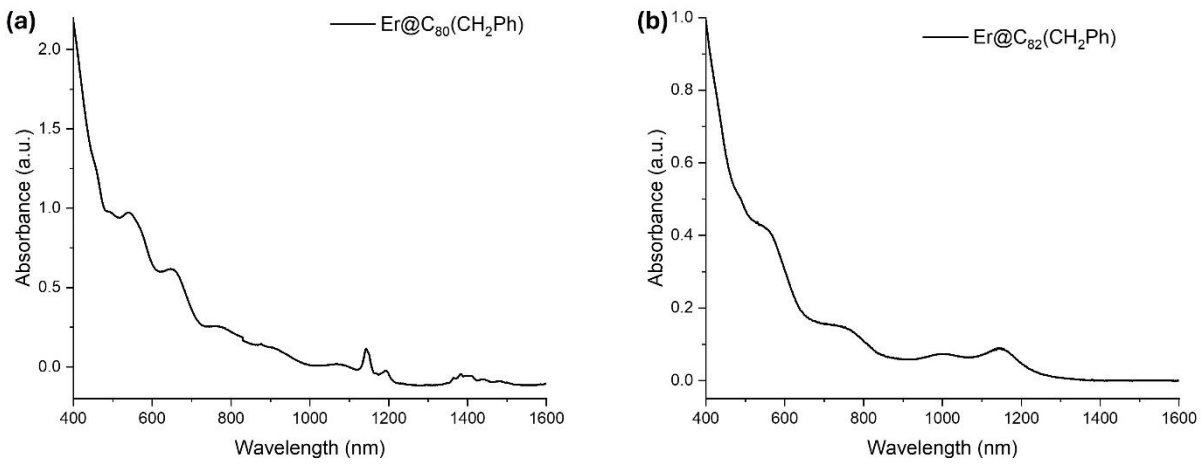


**Figure S3**. UV-vis-NIR absorption spectra of **(a)** Er@$C_{80}$($CH_2$Ph) and **(b)** Er@$C_{82}$($CH_2$Ph) measured in carbon disulfide.

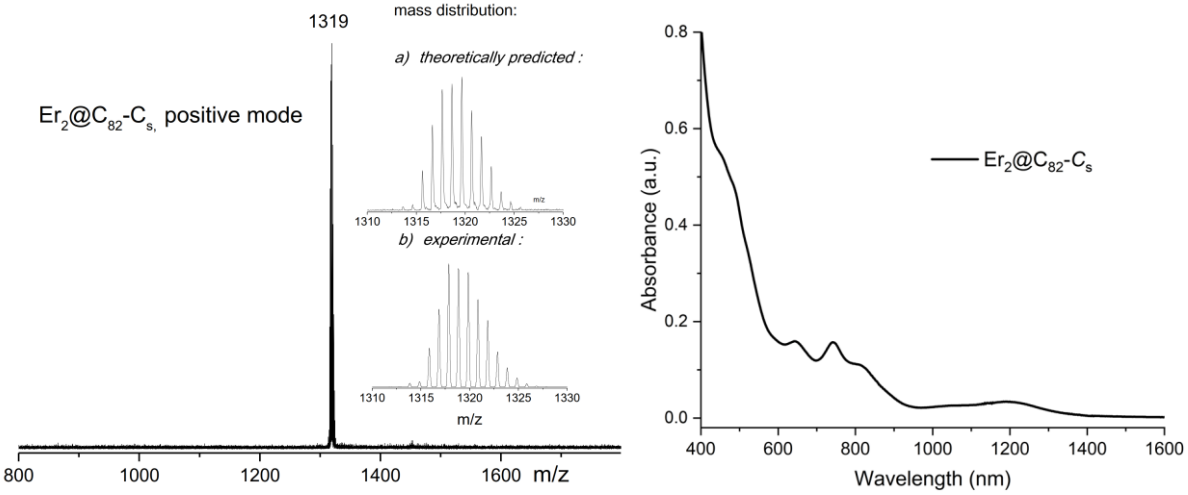


**Figure S4.** Mass-spectrum (left) and vis-NIR absorption spectrum (right) of $Er_2@C_s(6)$-$C_{82}$.

**Simulations of EPR spectra**

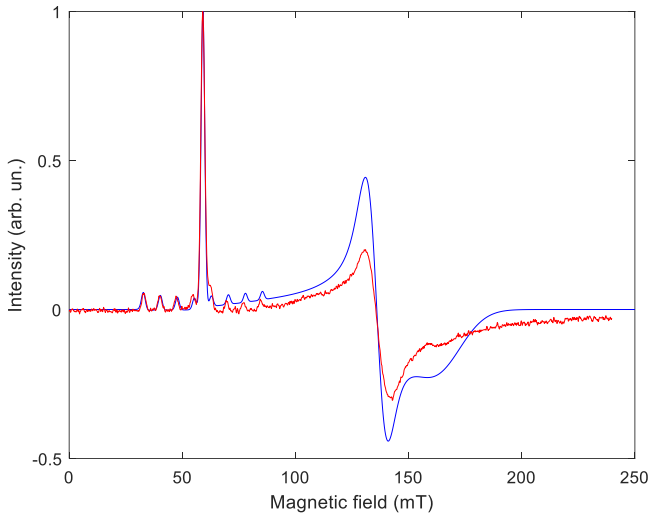


**Figure S5**. Experimental (red) and simulated (blue) EPR spectra of Er@$C_{80}$($CH_2$Ph); $a_x$ and $a_y$ are not considered since there is no observable hyperfine splitting in the range of $g_x$, $g_y$. Parameters of simulated spectrum: g = (4.2, 5.05, 11.625); $a_z$ = 1200 MHz, HStrain = (1500, 600, 300)

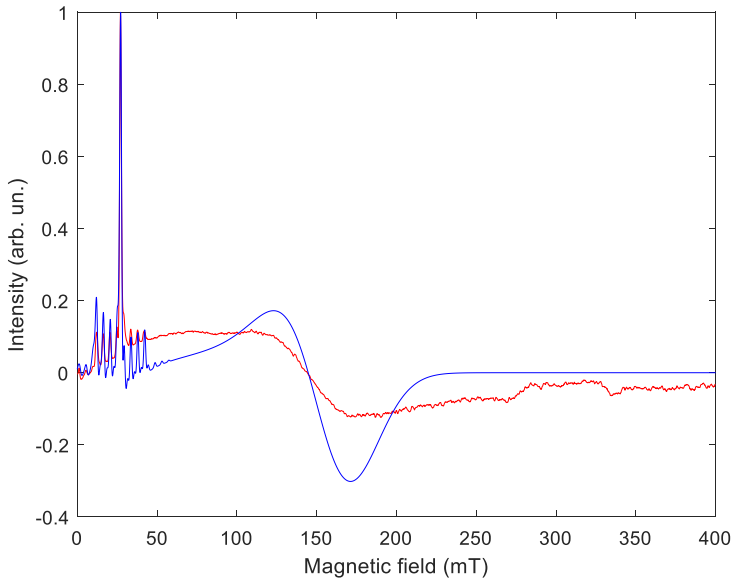


**Figure S6a**. Experimental (red) and simulated (blue) EPR spectra of $Er_2$@$C_{80}$($CH_2$Ph). Parameters of simulated spectrum: g = (4.3, 4.3, 25.00); $a_z$ = 1500 MHz, HStrain = (3000, 3000, 100).

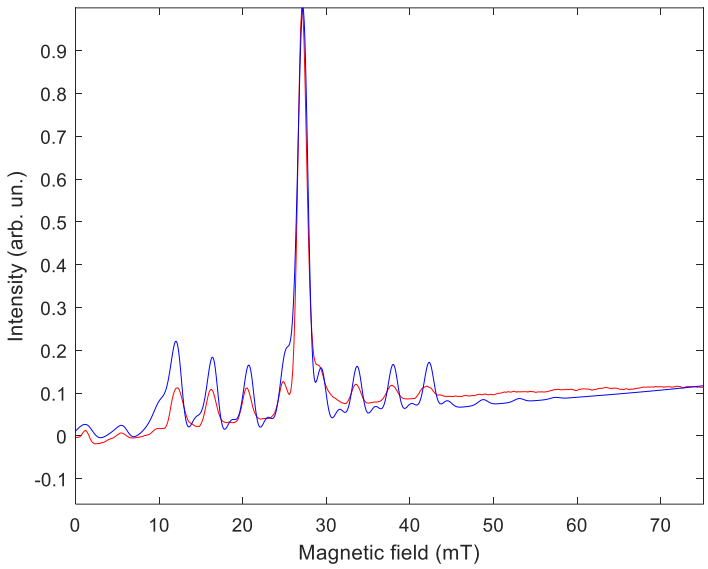


**Figure S6b**. Experimental (red) and simulated (blue) EPR spectra of $Er_2@C_{80}(CH_2Ph)$ in the low-field range.

**Computational studies of Er@$C_{80}$($CH_2Ph$) conformers**

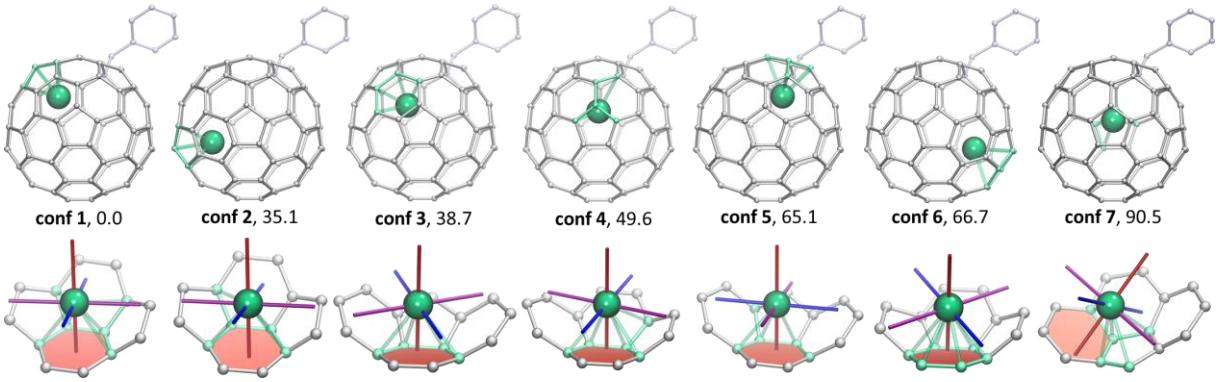


**Figure S7a.** Seven conformers of Er@$C_{80}$($CH_2Ph$) with their relative energies (kJ $mol^{-1}$) and metal-cage coordination with orientation of principal axes for KD1 pseudospin g-tensor in each of them. Principal values of g-tensors are listed in Table S1.

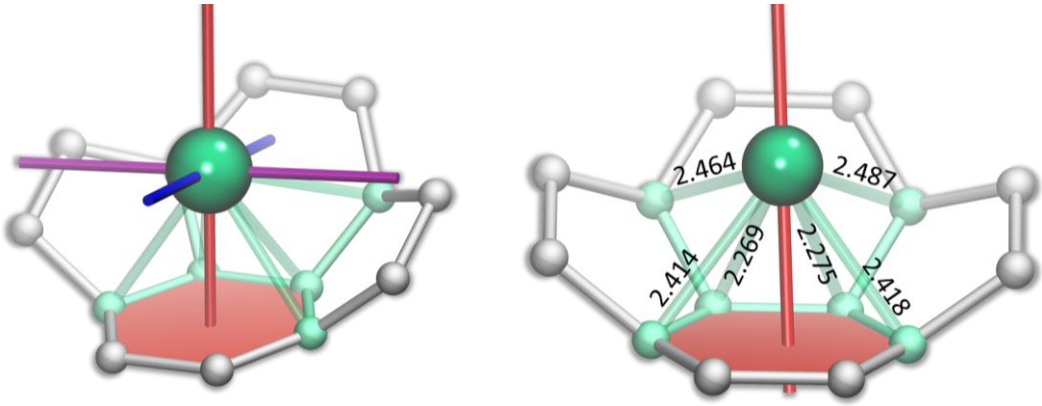


**Figure S7b.** Metal-cage coordination in **conf 1** with orientation of principal axes for KD1 pseudospin g-tensor (left, the same as Fig. 4c in the main text) and selected Er–C distances (Å) in DFT-optimized structure (right).

**Table S1.** Energies ($cm^{-1}$) of LF-split Kramers doublets (KDs) and KD1 g-tensors in conformers of Er@$C_{80}$($CH_2Ph$) computed with CASSCF/RASSI approach.

| | **conf 1** | **conf 2** | **conf 3** | **conf 4** | **conf 5** | **conf 6** | **conf 7** |
|---|---|---|---|---|---|---|---|
| KD1 | 0<br>2.4, 6.8, 9.7 | 0<br>1.5, 2.9, 11.3 | 0<br>0.2, 6.7, 9.1 | 0<br>2.5, 4.1, 11.9 | 0<br>0.5, 4.6, 11.6 | 0<br>0.8, 6.4, 8.4 | 0<br>1.0, 2.6, 13.4 |
| KD2 | 47 | 47 | 39 | 62 | 33 | 20 | 57 |
| KD3 | 105 | 76 | 80 | 91 | 78 | 76 | 114 |
| KD4 | 190 | 137 | 181 | 150 | 154 | 188 | 194 |
| KD5 | 220 | 196 | 232 | 208 | 184 | 222 | 208 |
| KD6 | 245 | 239 | 254 | 252 | 243 | 286 | 277 |
| KD7 | 384 | 319 | 406 | 361 | 374 | 347 | 384 |
| KD8 | 456 | 382 | 474 | 409 | 422 | 418 | 485 |

**Variable-temperature photoluminescence spectra of Er@$C_{80}$($CH_2$Ph)**

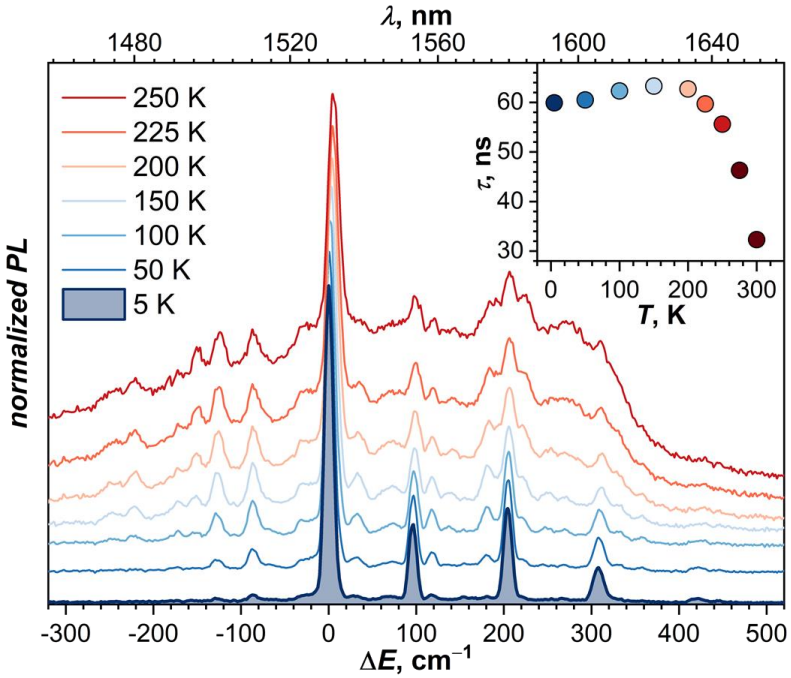


**Figure S8**. Photoluminescence spectra of Er@$C_{80}$($CH_2$Ph) measured at different temperatures in the range of the $^4I_{13/2} \rightarrow {}^4I_{15/2}$ transitions under laser excitation at 488 nm. The inset shows temperature dependence of the PL decay time of Er@$C_{80}$($CH_2$Ph). Each spectrum is normalized to the intensity of the most intensive peak at 1530 nm. Higher-temperature spectra show many features of comparable intensity, but the spectra become simpler at lower temperature.

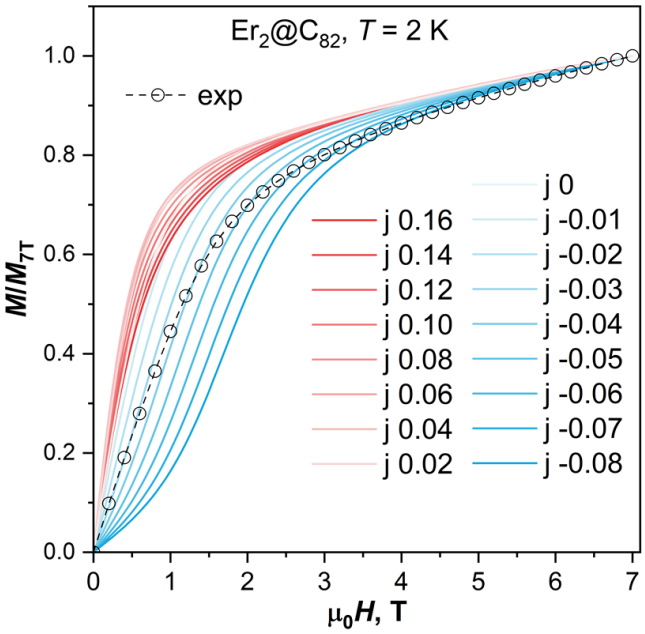


**Figure S9.** Magnetization curve of powder $Er_2@C_{82}$ measured by SQUID magnetometry at 2 K and compared to the curves calculated for different values of $j_{\mathrm{Er\text{-}Er}}$ (in $cm^{-1}$). The Hamiltonian used in simulations is: $\widehat{H}_{\mathrm{spin}} = \widehat{H}_{\mathrm{LF}'} + \widehat{H}_{\mathrm{LF}''} - 2j_{\mathrm{Er\text{-}Er}}\hat{J}_{\mathrm{Er}'}\hat{J}_{\mathrm{Er}''} + \widehat{H}_{\mathrm{ZEE}}$. For the sake of comparison, each curve is normalized to the magnetization at 7 T.